

Carderock Division, Naval Surface Warfare Center

Bethesda, Maryland 20084-5000

CARDIVNSWC-TR-95/021 August 1995

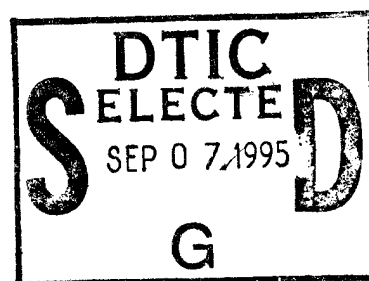
Hydromechanics Directorate
Research and Development Report

Computational Experiments on the Tracking of Vortices

by
H. J. Haussling

CARDIVNSWC-TR-95/021

Computational Experiments on the Tracking of Vortices



19950906 022

Approved for public release; distribution is unlimited.

THIS PAGE INTENTIONALLY LEFT BLANK

UNCLASSIFIED

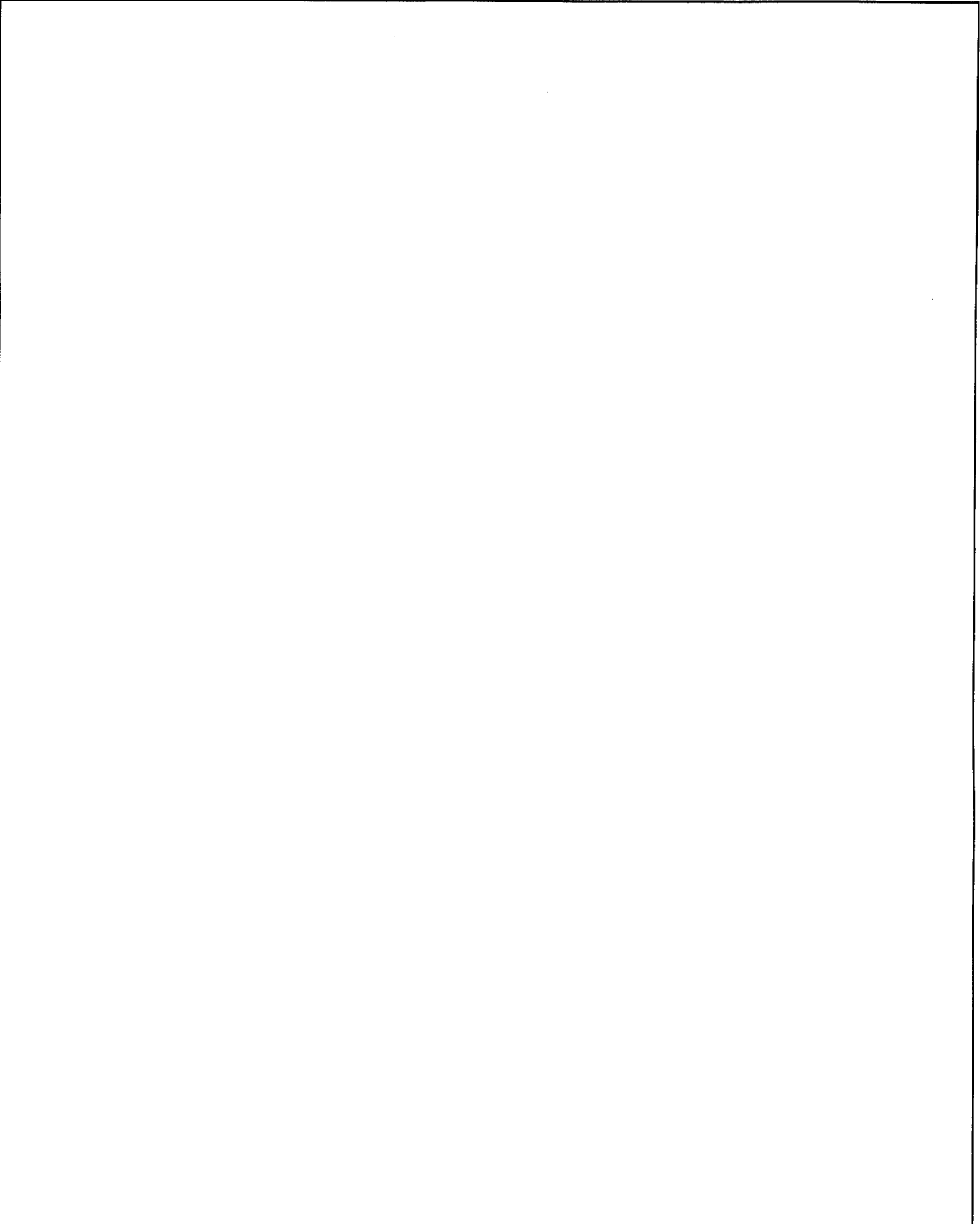
SECURITY CLASSIFICATION OF THIS PAGE

REPORT DOCUMENTATION PAGE

1a. REPORT SECURITY CLASSIFICATION UNCLASSIFIED		1b. RESTRICTIVE MARKINGS	
2a. SECURITY CLASSIFICATION AUTHORITY		3 DISTRIBUTION/AVAILABILITY OF REPORT Approved for public release; distribution is unlimited.	
2b. DECLASSIFICATION/DOWNGRADING SCHEDULE			
4. PERFORMING ORGANIZATION REPORT NUMBER(S) CARDIVNSWC-TR-95/021		5. MONITORING ORGANIZATION REPORT NUMBER(S)	
6a. NAME OF PERFORMING ORGANIZATION Carderock Division Naval Surface Warfare Center	6b. OFFICE SYMBOL (If applicable) Code 54	7a. NAME OF MONITORING ORGANIZATION	
6c. ADDRESS (City, State, and ZIP Code) Bethesda, MD 20084-5000		7b. ADDRESS (CITY, STATE, AND ZIP CODE)	
8a. NAME OF FUNDING/SPONSORING ORGANIZATION Office of Naval Research	6b. OFFICE SYMBOL (If applicable) ONR 334	9. PROCUREMENT INSTRUMENT IDENTIFICATION NUMBER	
8c. ADDRESS (City, State, and ZIP code) 800 N. Quincy St. Arlington, VA 22217-5660		10. SOURCE OF FUNDING NUMBERS PROGRAM ELEMENT NO. 602323N PROJECT NO. RB23H16 TASK NO. 2 WORK UNIT ACCESSION NO.	
11. TITLE (Include Security Classification) Computational Experiments on the Tracking of Vortices			
12. PERSONAL AUTHOR(S) Haussling, H. J.			
13a. TYPE OF REPORT Final	13b. TIME COVERED FROM _____ TO _____	14. DATE OF REPORT (Year, Month, Day) 1995, August	15. PAGE COUNT 33
16. SUPPLEMENTARY NOTATION			
17. COSATI CODES	18. SUBJECT TERMS (Continue on Reverse If Necessary and Identify by Block Number) Navier-Stokes Equations, Vortices, Vortex Computations		
19. ABSTRACT (Continue on reverse if necessary and identify by block number) A general-purpose viscous flow code, DTNS3D, has been used to compute the strength and trajectories of an isolated vortex and a vortex pair. Analytic solutions and previous computations are used to judge the accuracy of the three-dimensional steady-state results. It is possible to track, quite accurately, the decay and translation of these vortex structures. A byproduct of this study is some information on the limitations of the unsteady crossflow analogy and on the effect of axial velocity variations on vortex trajectories.			
20. DISTRIBUTION/AVAILABILITY OF ABSTRACT <input checked="" type="checkbox"/> UNCLASSIFIED/UNLIMITED <input type="checkbox"/> SAME AS RPT. <input type="checkbox"/> DTIC USERS	21. ABSTRACT SECURITY CLASSIFICATION UNCLASSIFIED		
22a. NAME OF RESPONSIBLE INDIVIDUAL Henry J. Haussling	22b. TELEPHONE (Include Area Code) (301) 227-1934	22c. OFFICE SYMBOL Code 542	

UNCLASSIFIED

SECURITY CLASSIFICATION OF THIS PAGE



DD FORM 1473, 84 MAR

UNCLASSIFIED

SECURITY CLASSIFICATION OF THIS PAGE

CONTENTS

	Page
ABSTRACT	1
ADMINISTRATIVE INFORMATION	1
INTRODUCTION	1
FLOW CODE DESCRIPTION	2
MATHEMATICAL FORMULATION	3
GRIDDING	4
RESULTS	6
Single Vortex with No Diffusion	6
Single Viscous Vortex with Uniform Axial Inflow	7
Single Vortex with Nonuniform Axial Inflow	11
Vortex Pair with Uniform Axial Inflow	17
Vortex Pair with Nonuniform Axial Inflow	20
CONCLUSIONS AND RECOMMENDATIONS	23
ACKNOWLEDGMENTS	23
REFERENCES	25

FIGURES

1. Typical grid in the y,z plane	5
2. Grid cross section in the x,z plane at $y = 0.5$	5
3. Computed and exact axial vorticity contours at $y = 0.5$ for a single vortex with no diffusion	7
4. Computed and analytic axial vorticity contours at $y = 0.5$ for a single vortex	8
5. Computed and analytic pressure contours at $x = 0.5$ for a single vortex	9
6. Computed and analytic axial vorticity contours at $y = 0.5$ for a vortex with $U_0 = 5$	10
7. Computed y -vorticity contours at $y = 0.5$ for a vortex with $U_0 = 5$	10

FIGURES (Continued)

	Page
8. Computed and analytic pressure contours at $x = 2.5$ for a vortex with $U_0 = 5$	11
9. Computed axial velocity contours at $x = 5$ for a vortex with $U_0 = 10$	12
10. Axial velocity distribution imposed at $x = 0$ for a single vortex	13
11. Computed and analytic axial velocity contours at $x = 5$ for a vortex with inflow corresponding to Fig. 10	14
12. Axial velocity distribution imposed at $x = 0$ for a single vortex	15
13. Computed and analytic axial velocity contours at $x = 5$ for a vortex with inflow corresponding to Fig. 12	15
14. Computed and analytic axial vorticity contours at $y = 0.5$ for a vortex with inflow corresponding to Fig. 12	16
15. Computed and analytic y -vorticity contours at $y = 0.5$ for a vortex with inflow corresponding to Fig. 12	16
16. Computed axial vorticity contours at $y = 0.5$ for a vortex pair	17
17. Vertical location of vortex pair versus time	18
18. Vertical location of vortex pair versus time computed with different grid resolutions	19
19. Vertical location of vortex pair versus time computed with different starting times	19
20. Computed axial velocity contours at $x = 12.5$ for a vortex pair	21
21. Computed axial velocity contours at $x = 25$ for a vortex pair	21
22. Vertical location of vortex pair versus time computed with different axial flow rates	22
23. Vertical location of vortex pair versus time computed with different axial flow distributions	22

Accesion For	
NTIS CRA&I	<input checked="" type="checkbox"/>
DTIC TAB	<input type="checkbox"/>
Unannounced	<input type="checkbox"/>
Justification	
By _____	
Distribution /	
Availability Codes	
Dist	Avail and / or Special
A-1	

ABSTRACT

A general-purpose viscous flow code, DTNS3D, has been used to compute the strength and trajectories of an isolated vortex and a vortex pair. Analytic solutions and previous computations are used to judge the accuracy of the three-dimensional steady-state results. It is possible to track, quite accurately, the decay and translation of these vortex structures. A byproduct of this study is some information on the limitations of the unsteady crossflow analogy and on the effect of axial velocity variations on vortex trajectories.

ADMINISTRATIVE INFORMATION

This report is submitted in partial fulfillment of Task 2, Hydrodynamic Wake Signatures in the Maneuvering and Control Project, RB23H16, in the Submarine Technology Block Program (ND3A/PE0602323N) for fiscal year 1994. The work described herein was sponsored by the Office of Naval Research (ONR 334) and performed by the Carderock Division, Naval Surface Warfare Center under Work Unit 5060-435.

INTRODUCTION

Vortices shed from objects moving through air and water as well as from fixed objects in flowing fluids are among the most striking and significant features of such flows. These flow structures have important implications in such areas as aircraft safety, sediment transport, and marine vehicle maneuvering and control. The abundant effects of these vortices are among the reasons that much effort has been put into the development of computer codes for the numerical solution of equations governing viscous fluid motions. The successful construction of such codes will allow the prediction of vortex generation and movement and will lead to a design capability for suppression or other modification of vortex flow features. Calculations are already being carried out regularly in many industries for flows around three-dimensional bodies. At Carderock Division, Naval Surface Warfare Center (NSWCCD) it is now quite common for viscous flow computations to be carried out in parallel with experimental efforts aimed at understanding and improving the flow about naval vehicles. These computations involve vortices shed from appendages, and indications are that the computer codes being used can track the vortices at least in a qualitatively correct manner. However, a large part of the ongoing validation of these codes must be a careful assessment of their ability to accurately predict vorticity production, concentration, diffusion, and convection. Only when such an assessment is complete will it be known to what extent and how these codes can be used as reliable research and design tools.

For these reasons, an effort was recently initiated at NSWCCD to validate the capability of existing methods and computer codes to accurately predict the generation and movement of vortices. This is a difficult task. Reliable experimental data are scarce. Most flows of interest are turbulent. When computational results are compared to measured data it is usually impossible to quantitatively divide the discrepancies into such categories as numerical error, measurement error, and shortcomings of turbulence models. To render this validation process more manageable, the effort has been divided into the nearfield task of vorticity production and vortex formation and the farfield task of vortex tracking. The work being reported falls into the farfield category.

This report is one of a series describing this validation effort. In previous documentation, Ohring and Lugt¹ showed that a careful numerical solution of the Navier-Stokes equations can yield an accurate prediction of the decay and movement of a pair of two-dimensional unsteady vortices. They demonstrated the accuracy of their results through comparison with previous analytic solutions. These results provide an excellent foundation for further efforts at method

and code validation. One of the goals of the present work is to reproduce their results in a three-dimensional steady flow solution. This makes sense only within the context of the unsteady crossflow analogy. This analogy states that two-dimensional unsteady solutions can be good approximations for three-dimensional steady flows as long as the crossflow velocities are dominated by the streamwise velocity, where the streamwise velocity is with respect to the reference frame in which the flow is steady.

If a method or code can accurately track a vortex pair, it should be able to handle vortices in more general situations. The code chosen is DTNS3D because of its availability, its ease of use, and its successes in previous applications. The approach is to separate the question of fundamental vortex tracking capabilities from the difficulties of turbulent flow modeling. Therefore, the code's turbulent flow models are initially turned off to provide laminar (or constant eddy viscosity turbulent) flow solutions. The first computations deal with an isolated vortex with and without diffusion. Comparisons are made with an analytic solution. Then the code is applied to the vortex pair, and comparisons are made to the results of Ohring and Lugt.¹ The computations are quite straightforward with the unsteady crossflow analogy indicating that the three-dimensional steady solutions should mimic the two-dimensional unsteady solutions quite closely. However, in three dimensions there is a third momentum equation, and hence a spatial variation in the streamwise velocity which must be handled by the flow solver. Thus a byproduct of this study is information gained about streamwise velocity distributions in vortices and the effect of such distributions on the validity of the unsteady crossflow analogy.

FLOW CODE DESCRIPTION

The DTNS codes were originally developed by Joseph Gorski at NSWCCD and have more recently been further developed and improved by Gorski and others. Details of the mathematical formulation on which they are based and of the numerical methods used in the codes have been presented numerous times elsewhere.²⁻⁵ Therefore, only a brief overview of the methods and features of the codes are presented here. The Navier-Stokes equations for steady incompressible flow are solved using pseudo-compressibility where an artificial time dependence is added to the continuity equation. The equations are then marched in time until a steady state solution is achieved. When the steady state is reached, all time derivative terms vanish and a solution of the equations for steady incompressible flow is obtained. The equations are discretized with the finite-volume formulation. Central differencing is applied to the viscous terms, but the high accuracy upwind total variation diminishing (TVD) scheme developed by Chakravarthy and Osher² is used on the convective terms. The Jacobian matrix of fluxes is used to create a set of eigenvectors and eigenvalues where fluxes are computed at the centers of cell surfaces. The upwind scheme divides the flux between neighboring cells into parts, each associated with an eigenvalue. Based on the signs of the eigenvalues, the fluxes are differenced in the appropriate direction to achieve unconditional stability. A third-order accurate scheme is chosen. Flux limiting is available to prevent oscillations from creeping into the solution during startup, but flux limiting is generally not needed for these incompressible flow computations. The codes include both Baldwin-Lomax and $k-\epsilon$ turbulence models. When the $k-\epsilon$ model is used, the TVD upwind differencing is also used on the $k-\epsilon$ equations.⁶ For laminar flow computations the turbulence models can be turned off. All viscous terms can be excluded if solution of the Euler equations is desired.

The equations resulting from the upwind differencing are solved in an implicit coupled manner with the use of either approximate factorization or an LU-ADI solver. The implicit part of the equations is discretized with a first-order accurate upwind scheme for the convective terms. This creates a diagonally dominant system that requires the inversion of block tridiagonal matrices. Since the implicit terms are zero upon convergence, the solution retains the high-order

accuracy of the explicit part of the equations. A spatially varying time step, based on the local eigenvalues, is employed.

MATHEMATICAL FORMULATION

Boundary value problems are formulated with a rectangular (x,y,z) coordinate system as required by the flow code. For the vortex pairs, all lengths are referred to their initial separation a_0 . For an isolated vortex this length scale is not present, and a different length would typically be used for nondimensionalization. But, in order to facilitate comparison of the results for the isolated vortices with those for the vortex pairs, a_0 is used for both cases. The characteristic velocity in both cases is κ_0/a_0 , where κ_0 is the vortex strength. Thus, in nondimensional form, the vortices will initially have a tangential velocity of one at a radial distance of one from their center, and the initial z (upward) velocity of the vortex pairs will be one. Calculations are carried out in parallelopiped boxes extending, in the streamwise direction, from an upstream face at $x = 0$ to a downstream face at $x = \ell$ where ℓ can be varied depending on how long a trajectory segment it is desired to compute. The vertical box sides are at $y = 0$ and $y = 20$ for the vortex pair calculations but the box contains $-20 < y < 20$ for calculations with a single vortex. For the pair computation, the bottom of the box slants upward from $z = -10$ at $x = 0$ to $z = -10 + (0.1)\ell$ at $x = \ell$. Similarly, the top slants upward with the same slope as the bottom from $z = 20$ at $x = 0$. This slant is included to accommodate the upward translation with downstream distance of the vortex pair. For the single vortex the top and bottom of the computational box are horizontal. A larger space is included in the box above the vortices, which are centered at $z = 0$ for $x = 0$, because of some concern that the flow at the slanted top boundary has a normal component directed into the flow region and hence this boundary may behave as an inflow boundary. No problems were noted with this boundary for any of the computations and it is believed that this precaution is unnecessary.

Within this box region, the Euler or Navier-Stokes equations are solved depending on whether it is desired to consider convective effects alone or to include diffusive effects as well. This solution is accomplished through execution of the DTNS3D code with turbulence models turned off to get a Navier-Stokes solution or with all viscous terms turned off to get an Euler solution. The dependent variables used by this code are u , v , w , and p , the velocities in the x , y , and z directions and the pressure, respectively. For this study these variables are interpreted as dimensionless quantities. At the inflow boundary, the three velocity components are specified

$$(u, v, w) = (U(y, z), V(y, z), W(y, z)) \text{ at } x = 0 \quad (1)$$

At the plane of symmetry, for the case of a vortex pair the symmetry conditions

$$\frac{\partial u}{\partial y} = 0, \quad \frac{\partial w}{\partial y} = 0 \text{ and } v = 0 \text{ at } y = 0 \quad (2)$$

are applied. At all other boundaries, the characteristic directions are such that simple first-order extrapolation can be applied to the velocities as a numerical approximation to:

$$\frac{\partial(u, v, w)}{\partial n} = 0, \quad (3)$$

where n represents the coordinate direction normal to the boundary. Pressure boundary conditions are not needed for the mathematical problem. For computational purposes first order extrapolation is applied to the pressure at all boundaries:

$$\frac{\partial p}{\partial n} = 0. \quad (4)$$

The pressure is fixed at $p = 1$ at one upstream corner of the box to eliminate the arbitrariness in the pressure definition.

Because this is a steady-state formulation, initial conditions are not needed for the mathematical statement of the problem. However, the numerical approach is iterative, and initial conditions are needed for the computations. Two basic initial conditions are utilized. In the first, the flow field is of constant pressure everywhere with uniform stream throughout except at the upstream boundary where the desired inflow velocity distribution is specified. Vortices trailing a body will be steady in a frame of reference translating with the body/vortex system. The uniform stream referred to is this translational velocity and is the velocity in the far field relative to this reference frame. In the second form of the initial conditions, a distribution of velocities and pressure is specified throughout the computational region. This distribution is selected to try to better approximate the anticipated steady solution. The first form of initial conditions leads to large initial streamwise gradients at the inflow boundary followed by a gradual spread of this disturbance throughout the region until a steady-state solution is achieved. The second form of initial conditions leads to a less dramatic adjustment of the initial vortex to its steady-state position, the details depending on the quality of the initial distribution imposed. The latter has the potential of leading to a numerical solution more rapidly while the former is more representative of the nature of the initial conditions encountered in practical applications. In preliminary computations, it is verified that the two initial conditions lead to essentially identical steady flow solutions.

GRIDDING

The vortices are close to, or exactly axisymmetric in the crossflow plane; therefore, the most efficient use of grid points would result from a grid based on polar-type coordinates about the vortex center. However, in applied calculations it is often necessary to track vortices that move on an unknown trajectory through a grid that is tailored to a body or other geometrical feature. For this work a grid is used that is rectangular in the crossflow plane to avoid excluding some of the difficulties that might be encountered through use of a grid which is not conformed to the vortex shape. However, a refinement is built into this grid to assure that increased resolution is present in the vortex cores at least for some distance downstream from the inflow boundary. A typical portion of a grid cross-sectional plane for the vortex pair is displayed in Figure 1. The minimum spacings are $\delta y = 0.0033$ and $\delta z = 0.0025$ centered at $y = 0.5$ and $z = 0.0$. The grid spacing expands logarithmically in both y and z directions. For an isolated vortex the grid extends to $y < 0$ and is symmetric about $y = 0.5$. A side view of an x,z grid plane at $y = 0.5$ for a vortex pair computation is shown in Figure 2. This grid slopes upward parallel to the top and bottom boundaries. Thus the region of fine resolution tends to follow the upward slope of the vortices. However, to the extent

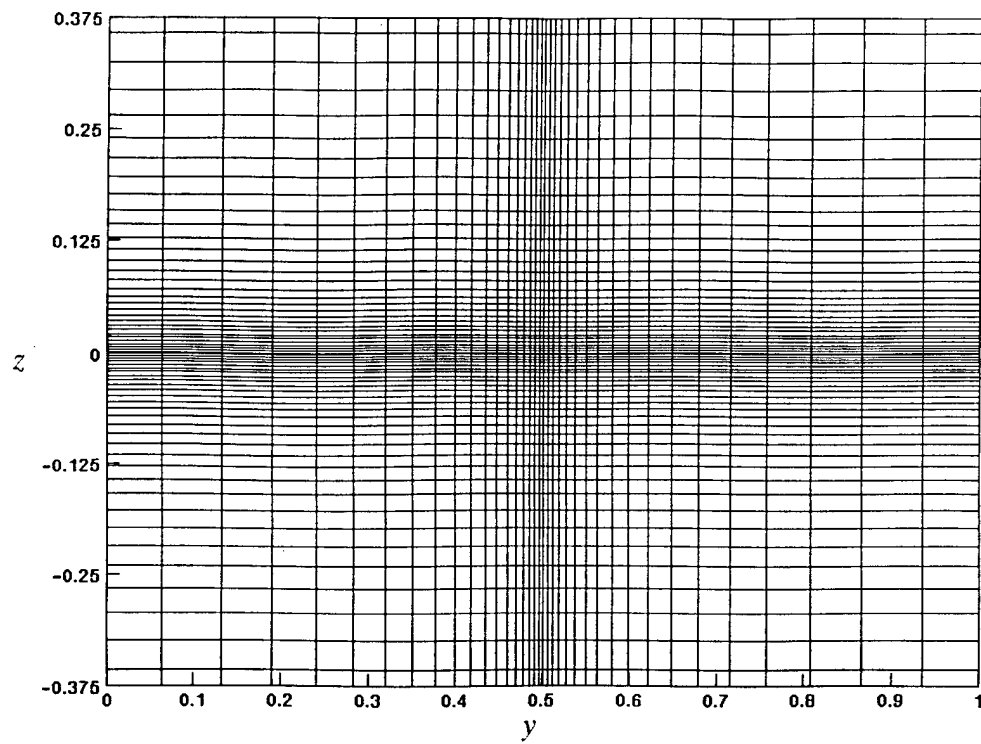


Fig. 1. Typical grid in the y, z plane.

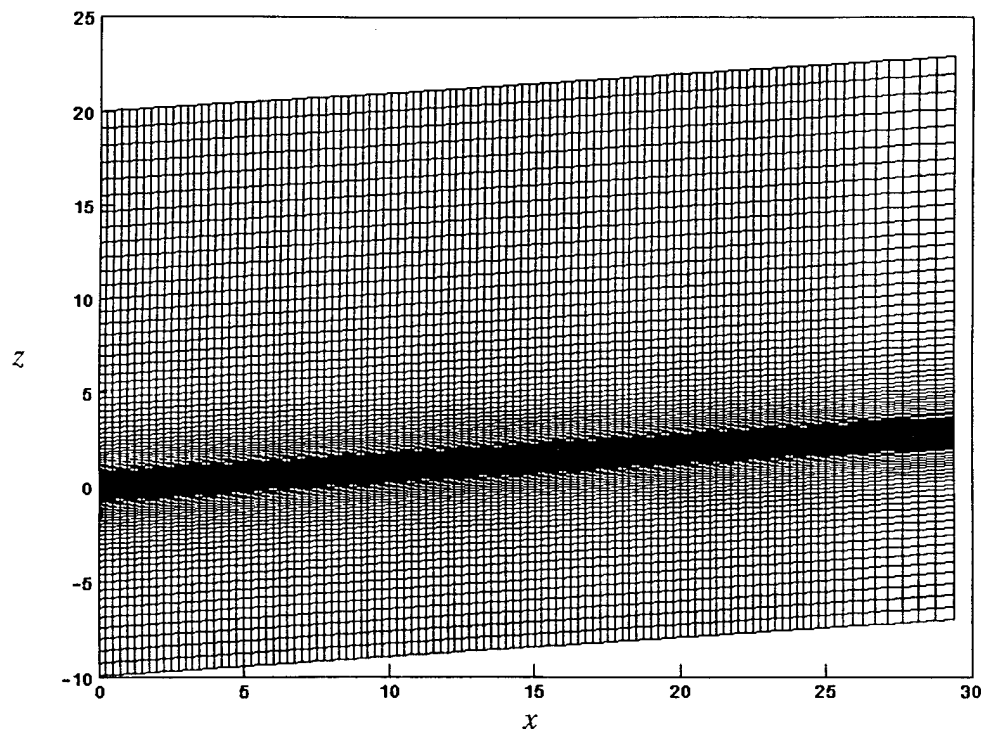


Fig. 2. Grid cross section in the x, z plane at $y = 0.5$.

that the upward slope of the vortices diminishes due to diffusion and three-dimensional effects, they will tend to drift away from the minimum spacing with distance x from the inflow boundary. The basic spacing in the streamwise direction is $\delta x = 0.25$. For the single vortex there are 21 planes separated by this spacing, extending from $x = 0.0$ to $x = 5.0$, which comprise the main region of interest. These are followed by another 10 planes where each succeeding spacing in the x -direction is increased by 10 percent over the previous spacing. These latter planes are used to remove the outflow boundary from the region of interest and thus minimize any deleterious effects of outflow boundary conditions. This box for the isolated vortex extends from $x = 0.0$ almost to $x = 9.0$ and is referred to as the short box. For vortex pair computations, the region of interest extends for 101 planes to $x = 25.0$. This is again followed by a 10-plane region of expanding x -spacing, which extends the box almost to $x = 29.0$. This box is referred to as the long box. In addition the vortex pair calculations are continued successfully through a similar box, with a region of interest from $x = 25.0$ to $x = 50.0$, by using the computed result at $x = 25.0$ as an inflow condition.

There are a total of $31 \times 81 \times 149 = 374,139$ points in the x -, y -, and z -directions, respectively, for the single vortex computations and $111 \times 61 \times 149 = 1,008,879$ points for the vortex pair computations.

RESULTS

SINGLE VORTEX WITH NO DIFFUSION

An isolated, axisymmetric vortex in the absence of diffusion should continue indefinitely in the streamwise direction with unchanged crossflow characteristics. In order to test the ability of the code to handle this rather simple case, the viscous terms are turned off and the code is run in its Euler equation mode. The crossflow velocities imposed at the inflow boundary correspond to Lamb's two-dimensional unsteady (decaying) vortex of initial strength κ where the vorticity ω is given by

$$\omega = (Re/2t)e^{-Rer^2/4t}, \quad (5)$$

evaluated at time $t = 2$ and for Reynolds number $Re = \kappa/v = 100$; where v is the kinematic viscosity, and $r^2 = (y-0.5)^2 + z^2$. Because the desired solution has all x -derivatives zero, it essentially should be independent of the streamwise velocity. A streamwise velocity of $u = U_0 = 10$ is imposed at the inflow plane in anticipation of the more complicated cases considered below.

The code is run in the small box with the above inflow condition and with two initial conditions, each for somewhat over 1000 iterations. Each iteration consumed about four minutes on a Convex 3840 computer. For an initial condition consisting of the exact solution, namely the dependent variables corresponding to Equation (5) extended throughout the x -direction, longitudinal cross-sectional plots of the vorticity contours at the vortex center are presented in Figure 3. Even with the highly expanded vertical scale relative to the horizontal scale, the computed contours agree quite well with the exact (horizontal) contours. This result shows that the code is capable of producing an excellent approximation to the exact solution for this simple case, at least when the initial condition is very close to the desired result. To better test the ability of the code to generate a solution from scratch, this case was rerun with a uniform stream (zero crossflow) initial condition. The extra work needed to develop the vortex throughout the box is reflected by the fact that the results for the first initial condition were essentially unchanged from iteration 200 to iteration 1000, while the computations for this second initial condition took about three times as long to converge. After about 600 iterations the results are essentially the same as those presented in Figure 3.

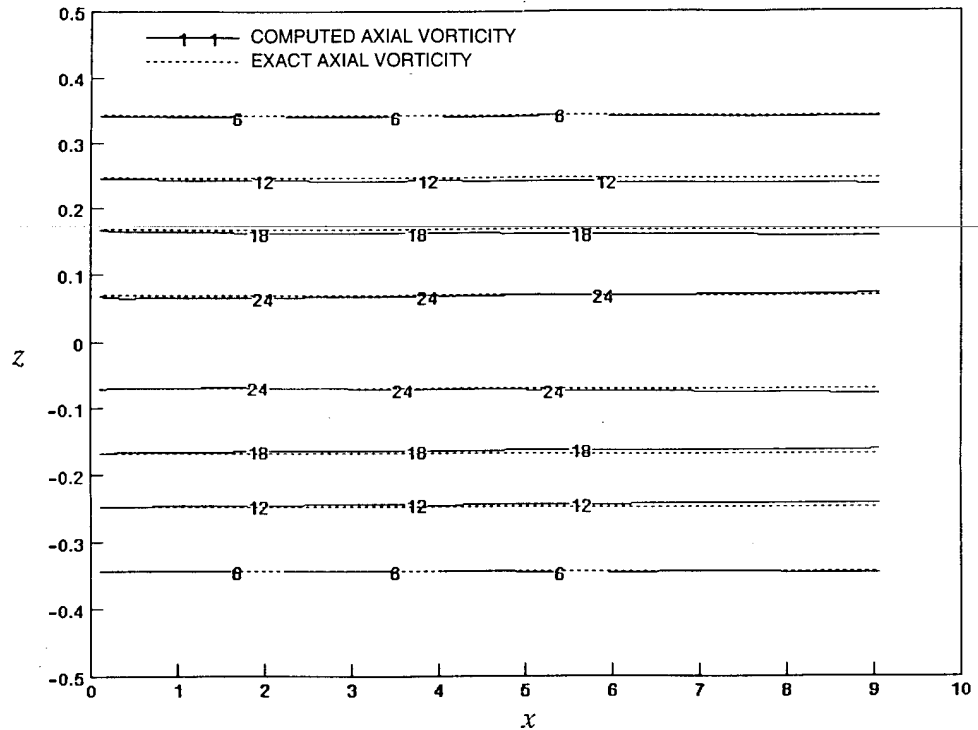


Fig. 3. Computed and exact axial vorticity contours
at $y = 0.5$ for a single vortex with no diffusion.

SINGLE VISCOUS VORTEX WITH UNIFORM AXIAL INFLOW

An isolated, axisymmetric vortex in the wake of flow past a body will, in reality, decay with distance from the body because of the effects of molecular or turbulent diffusion. This process can be handled in the laminar flow case by the Navier-Stokes equations, which can also be appropriate for turbulent flow if a constant eddy viscosity model is accurate. To test the capability of the code to handle such a decaying vortex, the computation of the above section is repeated with the viscous terms turned on so as to run the code in its Navier-Stokes mode. For this steady three-dimensional problem, there is no exact solution as in the previous case. However, Lamb's exact solution to the unsteady decay of a two-dimensional vortex provides a useful approximate solution as long as the unsteady crossflow analogy is valid. This analogy holds when the streamwise (axial) velocity is suitably large compared to the crossflow velocity components. This condition should be fulfilled as long as the axial velocity does not drop much below its inflow value ($U_0 = 10$). Then the crossflow fields become essentially independent of the axial flow field, and the three-dimensional steady solution can be usefully approximated by a corresponding two-dimensional unsteady solution. The inflow condition for the desired three-dimensional problem must be used as the initial condition for the two-dimensional problem. Since the inflow condition used for the current study is Lamb's solution at $t = t_0 \equiv 2$, the complete two-dimensional unsteady solution will be given by Equation (5). The approximate three-dimensional steady solution is then obtained by replacing t in Lamb's solution (Equation 5) according to

$$t - t_0 = x/U_0. \quad (6)$$

The approximate solution obtained in the above manner is used as the initial condition for the computation. After a few hundred iterations a converged solution is obtained. The computed solution must agree with the analytic solution near the inflow plane because of the inflow boundary conditions. However, the computed solution will agree with the analytic solution farther downstream only to the extent that the code accurately reproduces the diffusion process of the governing equations. To assess the accuracy of the code, comparisons of the two solutions are made in Figures 4 and 5. Figure 4 displays a comparison of axial vorticity contours in a longitudinal plane, and Figure 5 displays pressure contours in a cross section at $x = 5$. These two comparisons display excellent agreement of the computed solution with the approximate analytic solution. This good agreement demonstrates both the accuracy of the code and the validity of the unsteady crossflow analogy.

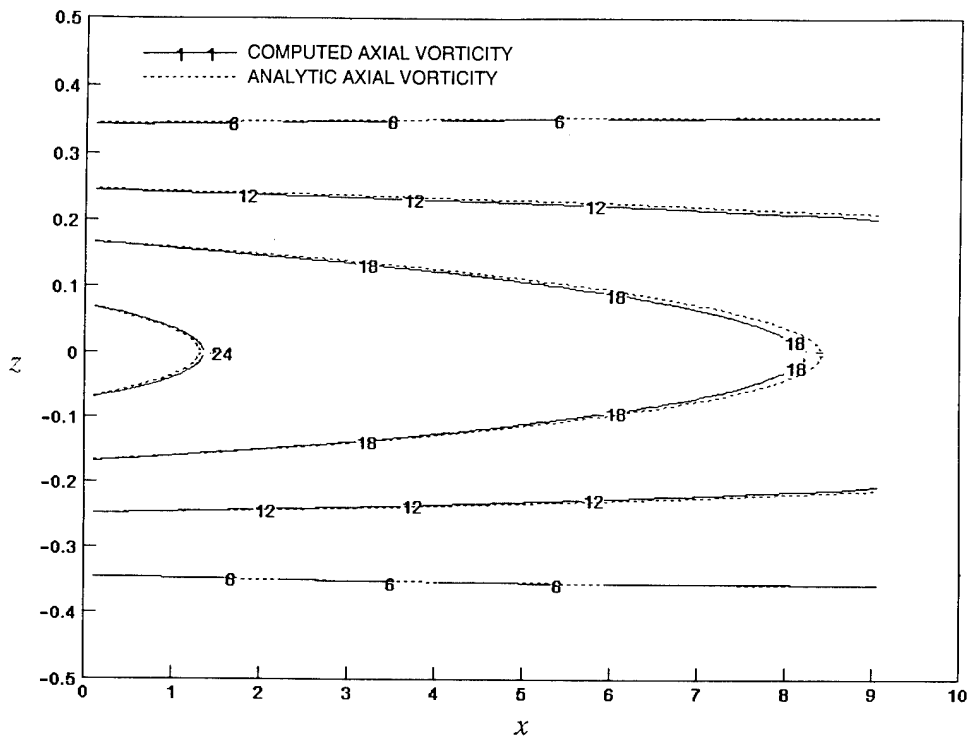


Fig. 4. Computed and analytic axial vorticity contours at $y = 0.5$ for a single vortex.

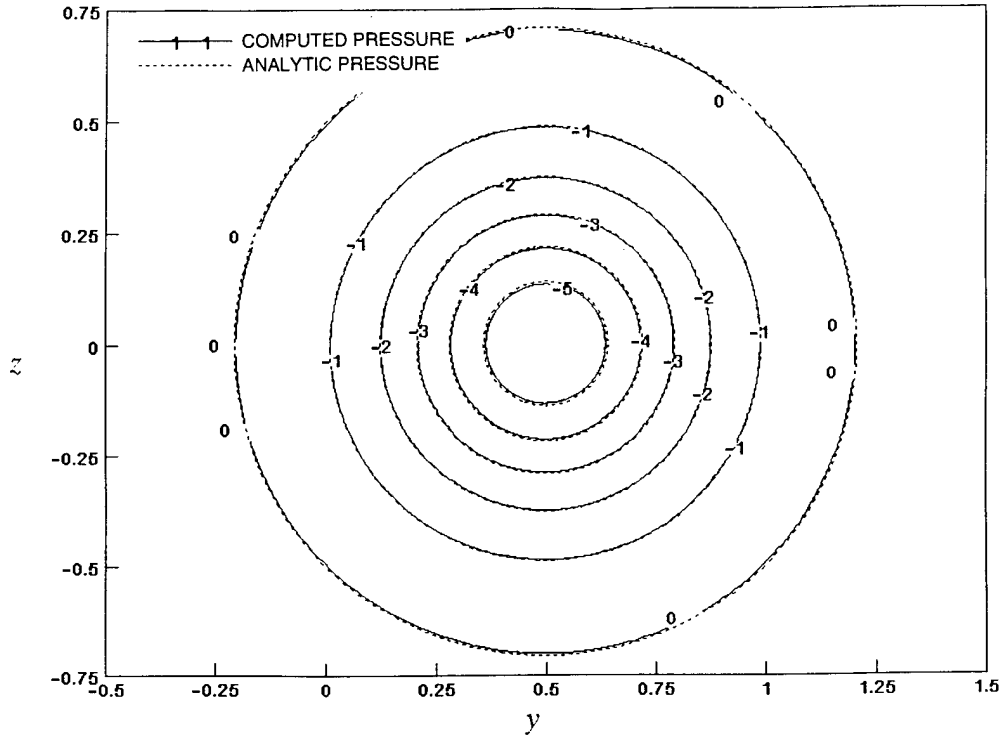


Fig. 5. Computed and analytic pressure contours at $x = 0.5$ for a single vortex.

The inflow axial velocity, $U_0 = 10$, was chosen to assure the validity of the unsteady crossflow analogy. It is possible to explore the limitations of this validity by imposing different inflow values. To this end the computations are repeated with an inflow condition of $U_0 = 5$. Figure 6 shows the resulting axial vorticity contours in the vortex centerplane compared with the analytic solution based on the unsteady crossflow analogy. Note that the length of the computational box has been halved in correspondence with the halving of the axial velocity. It is seen that the close agreement of Figure 4 has been lost. Evidently three-dimensional effects are large enough that the unsteady crossflow analogy is less accurate. It appears that the vortex dissipates more rapidly than for the case with larger axial velocity. Actually the dissipation is the same, but axial vorticity is converted to tangential vorticity. The generation of tangential vorticity is demonstrated in Figure 7, a plot of y -vorticity, which corresponds to tangential vorticity in the vertical vortex centerplane. These three-dimensional steady results show tangential vorticity increasing in the x -direction throughout the computational box. The unsteady crossflow solution does not account for such conversion of vorticity from one component to another.

Figure 8 displays a comparison of pressure contours in the cross section at $x = 2.5$. This comparison can be contrasted directly with that of Figure 5 for the larger axial flow. In spite of the deterioration with decreasing axial flow of the unsteady crossflow analogy, it still provides what might be a useful approximation for many purposes. It is not possible to draw a general conclusion on a precise limit on the utility of this approximation.

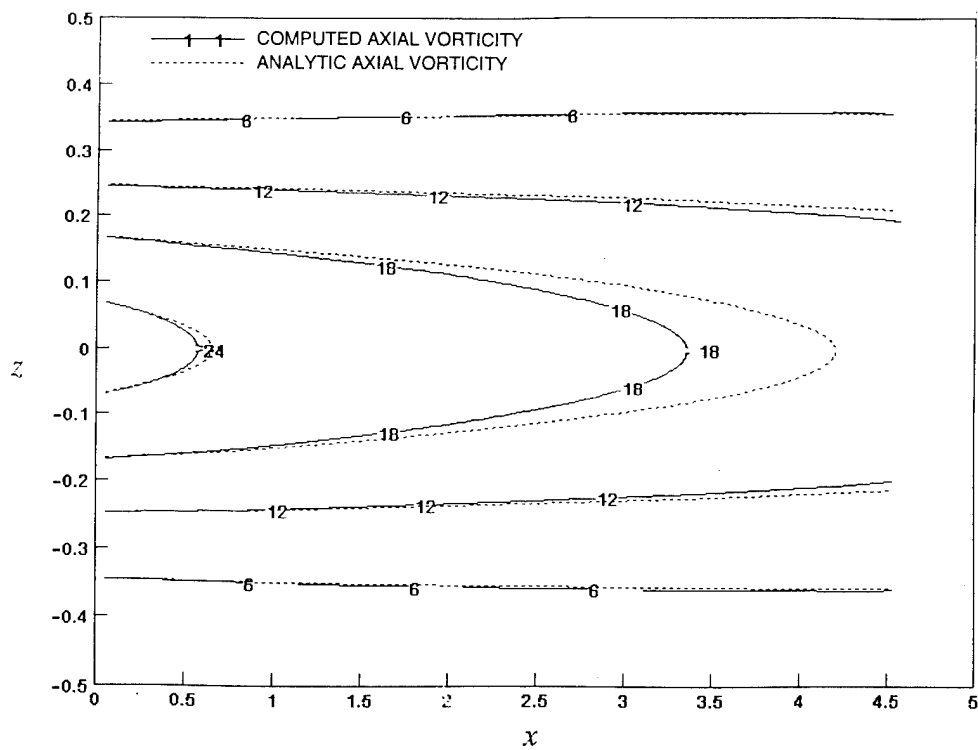


Fig. 6. Computed and analytic axial vorticity contours at $y = 0.5$ for a vortex with $U_0 = 5$.

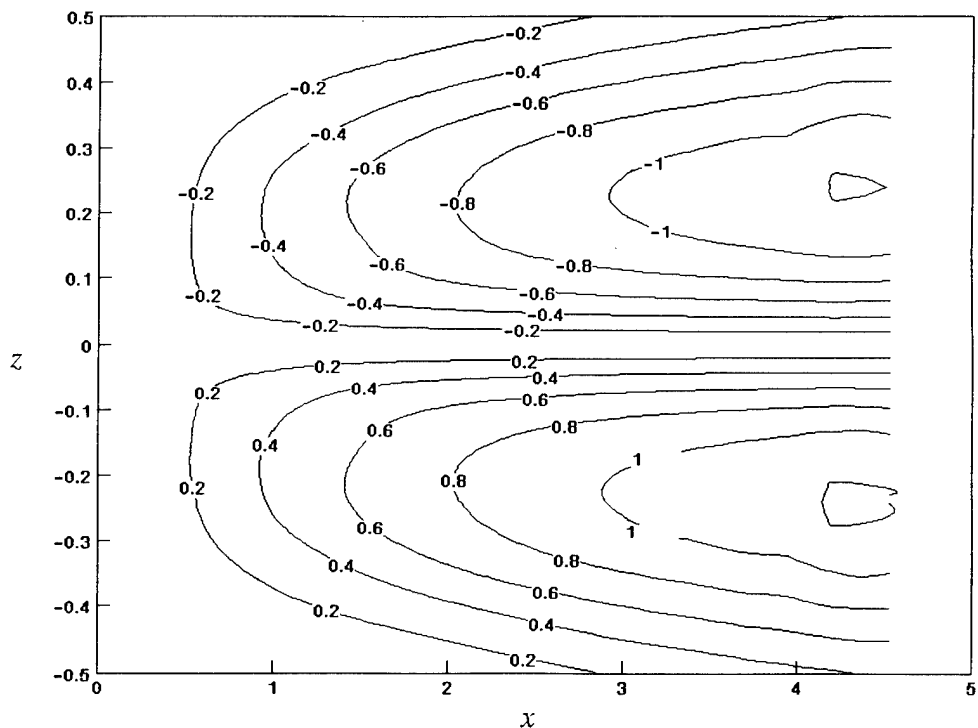


Fig. 7. Computed y -vorticity contours at $y = 0.5$ for a vortex with $U_0 = 5$.

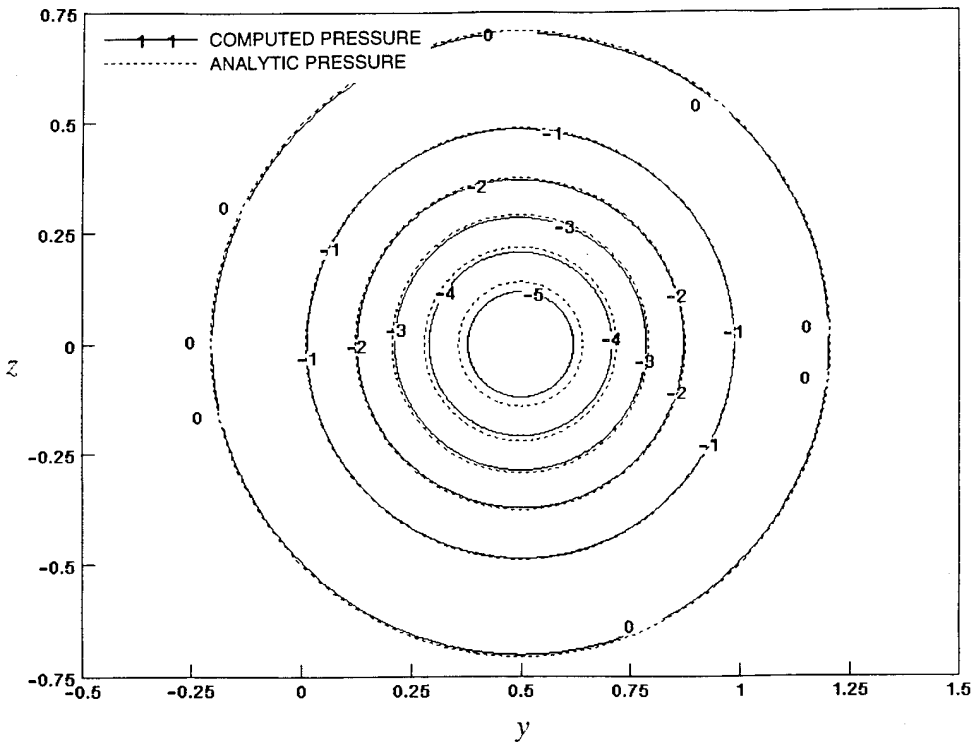


Fig. 8. Computed and analytic pressure contours at $x = 2.5$ for a vortex with $U_0 = 5$.

SINGLE VORTEX WITH NONUNIFORM AXIAL INFLOW

Even when the unsteady crossflow analogy is valid, there is a third momentum equation (for axial momentum) that must be satisfied in the three-dimensional case. Since the pressure distribution changes as the vortex decays, there are streamwise pressure gradients. These appear in the axial momentum equation, and hence they must be balanced by gradients of the axial velocity. These gradients affect the crossflow solution through the other momentum equations but only negligibly as long as the conditions of the crossflow analogy are not violated. The computed axial velocity contours at $x = 5$ for the flow of the previous section with inflow $U_0 = 10$ are displayed in Figure 9. The deviation from the inflow velocity is around one percent. The deviation of the contours from axisymmetric is due to numerical error, which, not surprisingly, is apparent at these low axial velocity variation levels.

It would seem that any inflow distribution of axial velocity can be specified and a suitable Navier-Stokes solution can be generated. If the axial velocity dominates the crossflow velocities throughout the region, then the crossflow field will be essentially the two-dimensional unsteady solution and will be independent of the axial inflow. Batchelor⁷ derived an approximate solution for the axial flow distribution based on the crossflow analogy. According to this solution the axial flow is given by

$$u = U_0 - (Re/8x) \log(U_0 Re x) Q_1(\eta) + (Re/8x) Q_2(\eta) - C(Re/8x) Q_1(\eta), \quad (7)$$

where

$$\eta = Re U_0 r^2 / 4x, \quad (8)$$

$$Q_1(\eta) = e^{-\eta}, \quad (9)$$

and

$$Q_2 = e^{-\eta} [\log \eta + ei(\eta) - 0.807] + 2ei(\eta) - 2ei(2\eta). \quad (10)$$

The function ei is related to the function Ei which is tabulated by Abramowitz and Stegun⁸ by

$$ei(\eta) = -Ei(-\eta). \quad (11)$$

The quantity C appearing in Equation 7 is a constant that can be chosen to adjust the solution to approximate a desired inflow.

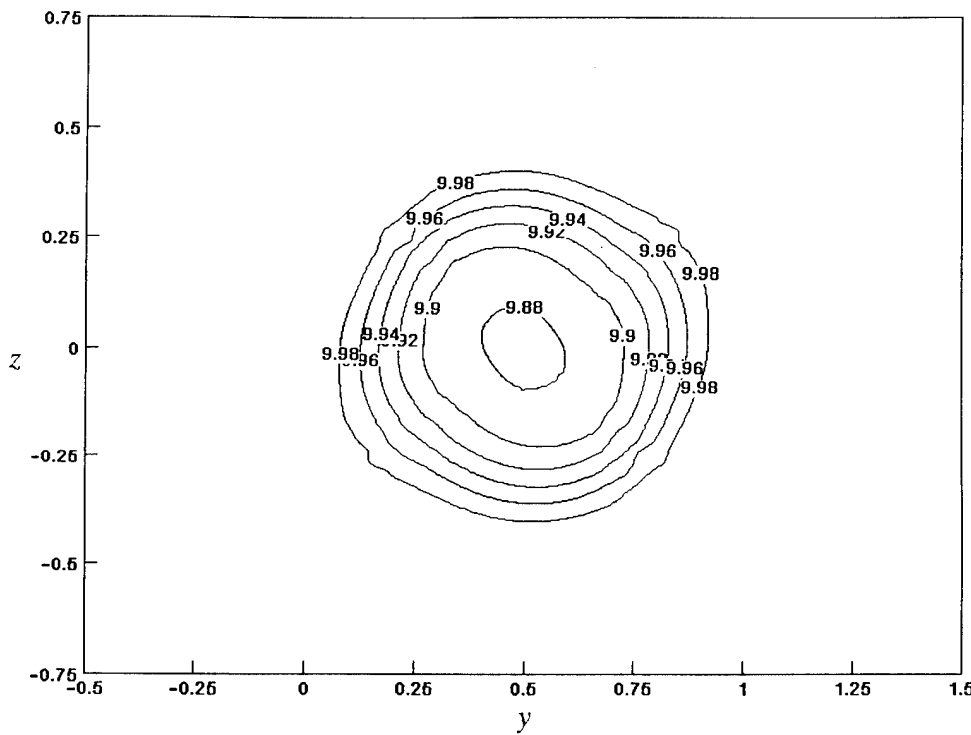


Fig. 9. Computed axial velocity contours at $x = 5$ for a vortex with $U_0 = 10$.

Equation 7 is used to verify the code's ability to accurately compute the axial velocity distribution. For $U_0 = 10$ that equation yields $u = U_0 = 10$ far from the vortex core. The constant C is chosen to yield a desired value of u at the center of the vortex, $r = 0$, at the inflow plane, $x = 0$. Initially, C is chosen such that the inflow axial velocity falls 10 percent, from its farfield value to 9 at the vortex center. The resulting inflow axial velocity distribution is shown in Figure 10. Corresponding velocity contours at $x = 5$ are shown in Figure 11. It is seen that both the computations and the approximate analytic solution display an increase in the streamwise direction of the axial velocity at the center. The analytic solution shows an increase from 9.0 at $x = 0$ to almost 9.1 at $x = 5$, while the numerical results show an increase to a value somewhat higher than 9.1. Apart from such slight differences, the computed and analytic solution agree quite well. The computed and analytic vorticity and pressure contours agree even more closely than the axial velocities with no difference noticeable between the two solutions when they are plotted on the scale of Figure 11. The small differences in the axial velocity contours are attributed to a slight breakdown of the unsteady crossflow analogy due to the axial velocity variations, and hence show the limitations of the approximate analytic solution. This explanation is verified by repeating the computations for an inflow axial velocity which varied only 1 percent from the farfield to the vortex center, in which case the axial velocity contours from the two solutions at $x = 5$ fall on top of each other when plotted as in Figure 11.

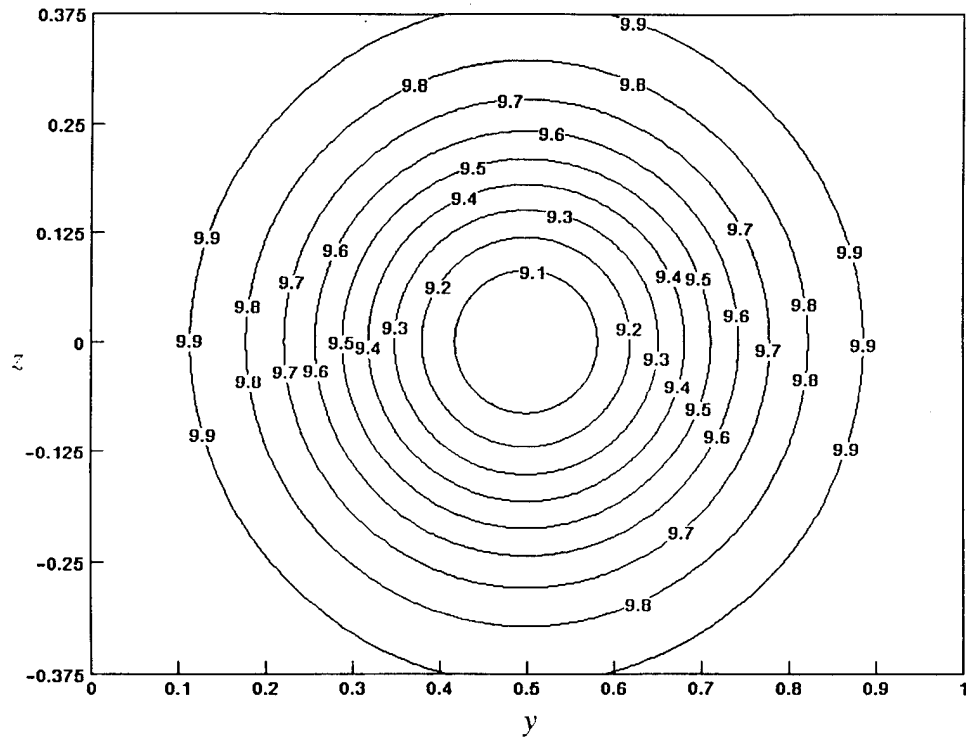


Fig. 10. Axial velocity distribution imposed at $x = 0$ for a single vortex.

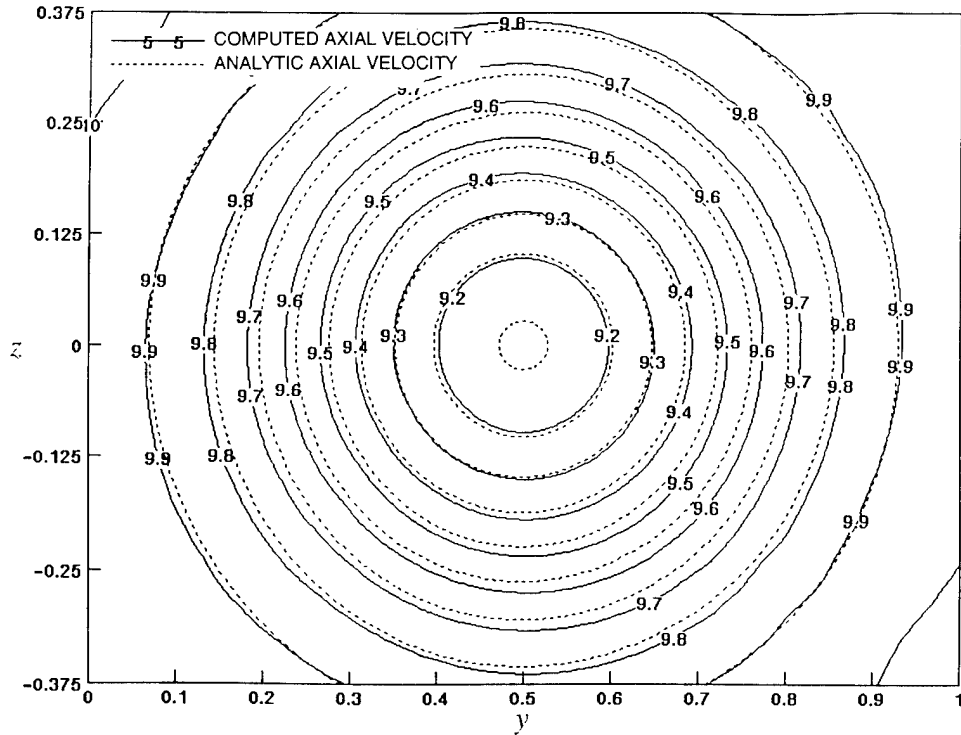


Fig. 11. Computed and analytic axial velocity contours at $x = 5$ for a vortex with inflow corresponding to Fig. 10.

It is possible to explore the effects of large axial flow variations through the computational approach beyond the limits of usefulness of the analytic solution. To this end computations are carried out with an inflow axial velocity distribution that varies 100 percent from 10 in the farfield to 0 at the center. This inflow distribution is shown in Figure 12. Computed and analytic velocity contours at $x = 5$ are plotted in Figure 13. The difference between the solutions is much larger here than for the previous case of smaller axial flow gradient. The axial velocity minimum at the center is about 1.9 according to the analytic solution but about 4.4 in the numerical results. The crossflow field is also different at $x = 5$ for the two solutions. Figure 14 shows a longitudinal section of axial vorticity contours for the computations and the analytic solution. The two flow fields agree at $x = 0$, and both solutions start there with a maximum vorticity of about 25. However, the maximum grows quickly with downstream distance x to a value of almost 42 in the computations, while the analytic solution does not exhibit this growth. Plots of the y component of vorticity are shown in Figure 15. This component is rather large at the inflow due to the axial velocity gradient there. The computed results show a rapid loss of y -vorticity with downstream distance. Evidently tangential vorticity is rapidly converted to axial vorticity for a short distance downstream from the inflow plane. Clearly, this case is well beyond the range of usefulness of the unsteady crossflow analogy which accounts for convection and diffusion of the two vorticity components but, as mentioned previously, cannot account for transfer between the components.

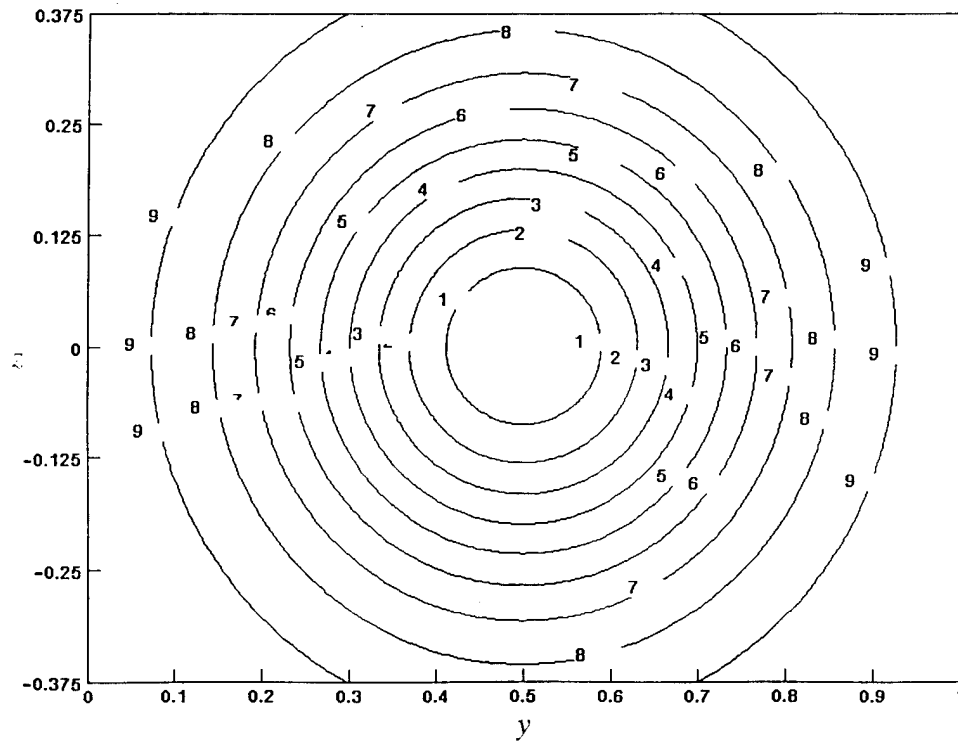


Fig. 12. Axial velocity distribution imposed
at $x = 0$ for a single vortex.

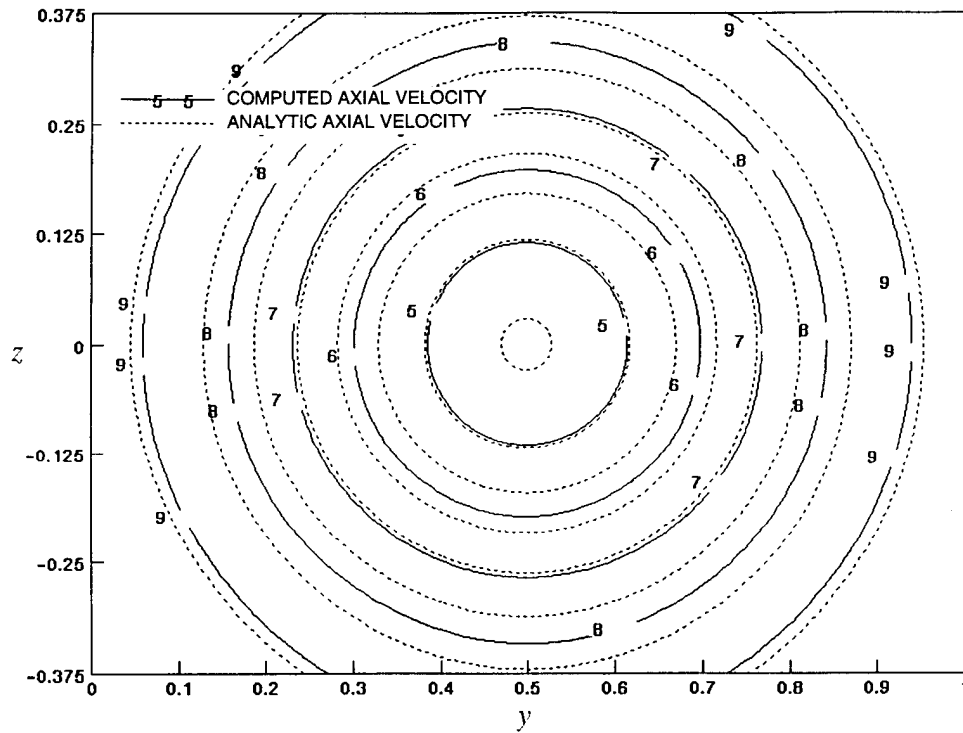


Fig. 13. Computed and analytic axial velocity contours at $x = 5$
for a vortex with inflow corresponding to Fig. 12.

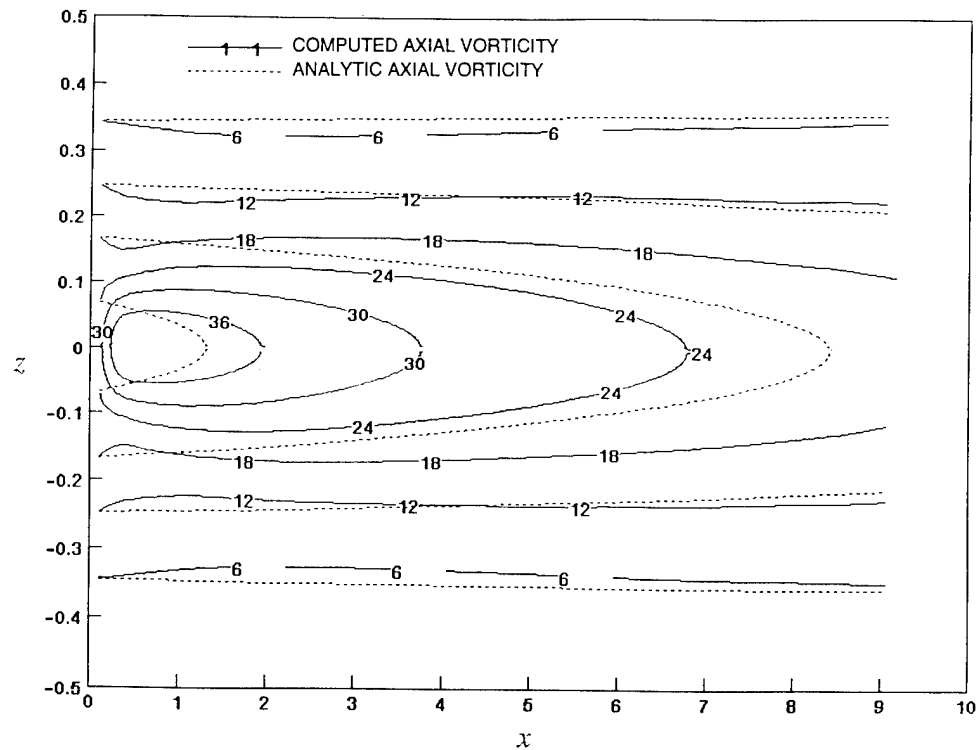


Fig. 14. Computed and analytic axial vorticity contours at $y = 0.5$ for a vortex with inflow corresponding to Fig. 12.

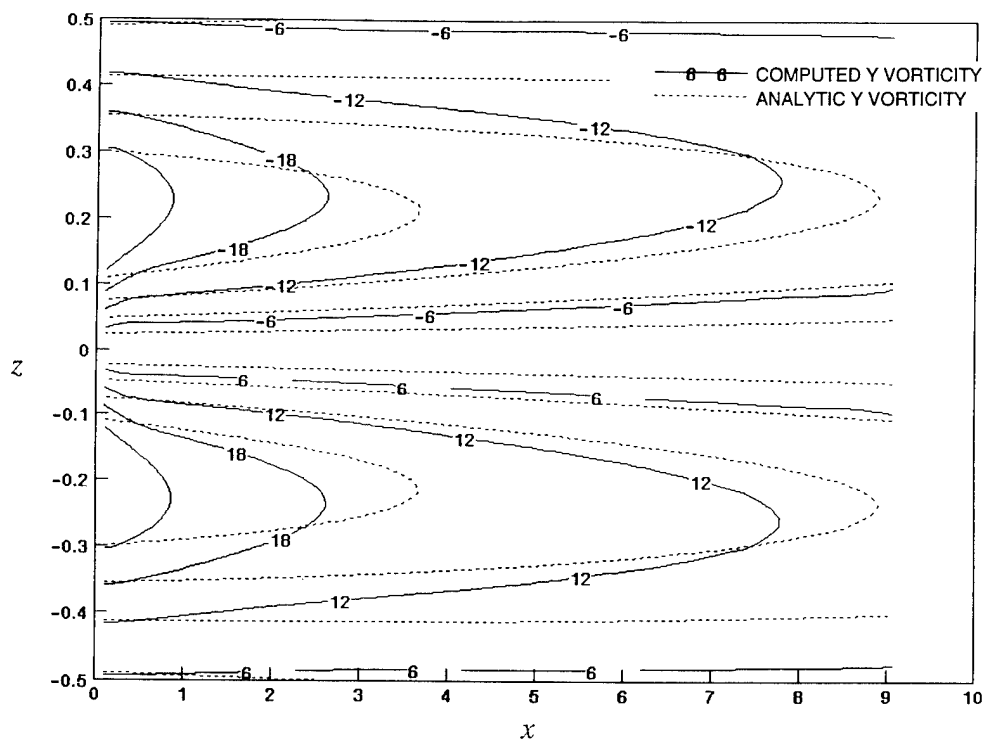


Fig. 15. Computed and analytic y-vorticity contours at $y = 0.5$ for a vortex with inflow corresponding to Fig. 12.

VORTEX PAIR WITH UNIFORM AXIAL INFLOW

A vortex pair will exhibit the convective effect of each vortex on the other in addition to the effects of diffusion. To test the ability of the code to cope with both effects simultaneously the code is run in its laminar flow mode with $Re = 100$ and with the Lamb vortex pair at $t_0 = 2$ and uniform axial velocity as the inflow condition. Calculations have been carried out in the long box. After convergence is achieved, the results at $x = 25$ are used as inflow conditions to a similar box to continue the solution to about $x = 50$ in the streamwise direction. The continuation of the solution in this manner works quite well. There is not an accurate analytic solution for comparison in this case. However, the excellent two-dimensional unsteady computational results of Ohring and Lugt¹ can be used.

A plot of the axial vorticity contours in the longitudinal centerplane of one of the vortices is presented in Figure 16. The vortex moves upward because of convection. At the same time diffusion acts to spread the vorticity and reduce its maximum. This results in a downward curvature of the vortex which increases with downstream distance and is most visible in the upper 5 level contour. This behavior represents a reduction in rise-velocity and is clearly visible in the plot in Figure 17 where the approximate vertical location of the pair is plotted versus time. This rise history is compared with the results of Ohring and Lugt and with the rise history for a pair of (inviscid) point vortices. The oscillations in the current results, most visible at the later times, are a result of the rather crude method for approximating the vortex location. The vorticity is computed at grid cell centroids. The location of the vortex is taken to be at the grid cell centroid with the largest vorticity value. The vortex moves upward with distance x , as does the grid. Therefore, the maximum vorticity tends to appear in the same cell for several successive constant x planes. When the vortex has moved enough for the maximum vorticity to appear in a different grid cell at one x plane than in the previous plane, there appears a kink in the rise history. The oscillations grow

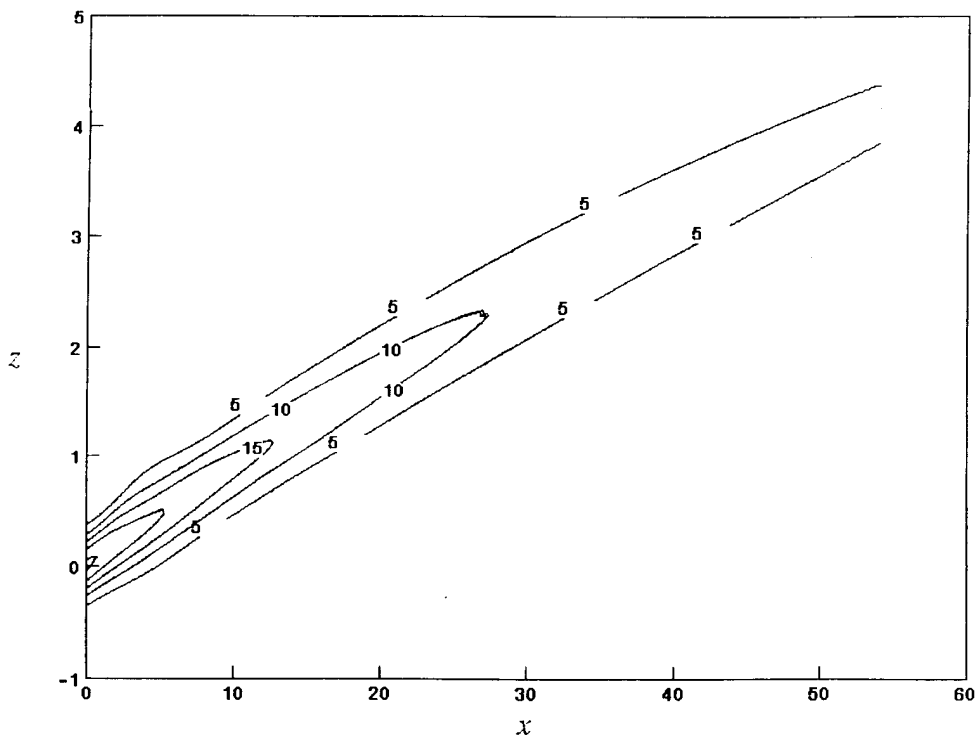


Fig. 16. Computed axial vorticity contours at $y = 0.5$ for a vortex pair.

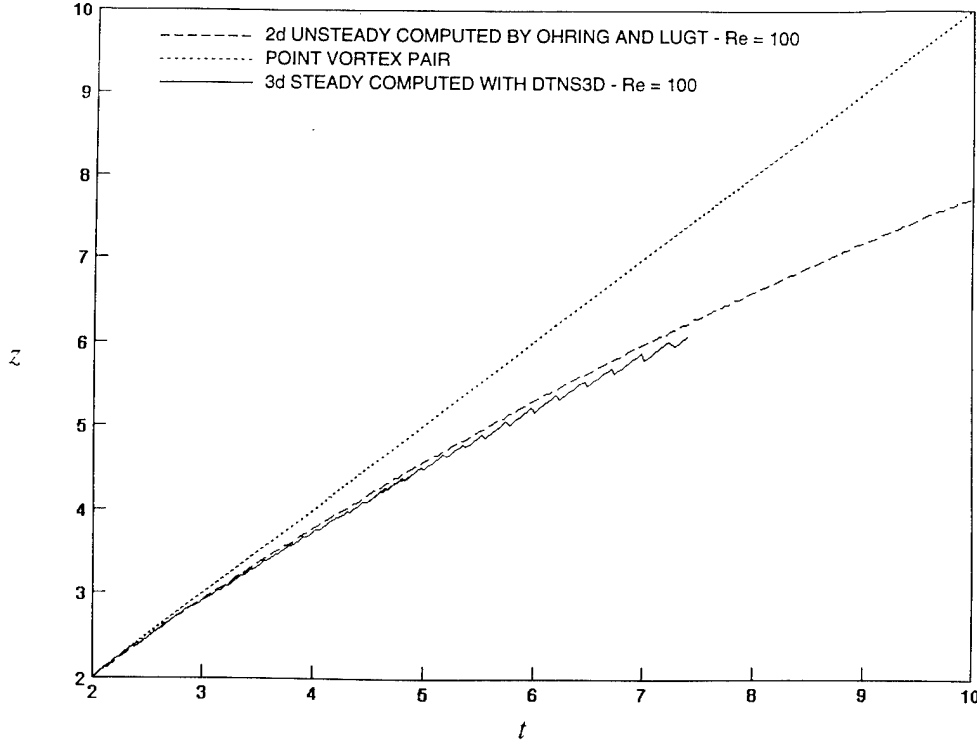


Fig. 17. Vertical location of vortex pair versus time.

with time since the vortices gradually move away from the area of maximum grid resolution, which was chosen to follow the point vortex pair trajectory. A smoother rise history could be generated, if warranted, by better estimating the location of the vorticity maximum within a grid cell. The current results predict a rise-velocity that is slightly lower than that of Ohring and Lugt. Possible explanations for this include numerical inaccuracies, differences in starting conditions, and real differences between the two-dimensional and three-dimensional flows.

To assess the impact of grid spacing on the results, the first long box computation is repeated with every other grid point removed in all three directions. Except for a further loss of smoothness the resulting rise-history curve is essentially unchanged, as seen in Figure 18 where it is compared with that for the original grid.

To assess the effect of starting conditions on the results, the first long box computation with the vortex pair is repeated with an inflow condition corresponding to a pair of Lamb vortices at $t_0 = 1.5$. The resulting rise history is presented in Figure 19, where it is compared with the previous results for $t_0 = 2$ and with the results of Ohring and Lugt for which $t_0 = 0.2$. The current results for the two starting conditions are quite close. Moreover, the slight dependence on t_0 is in the wrong direction to provide an explanation of the deviation from the results of Ohring and Lugt.

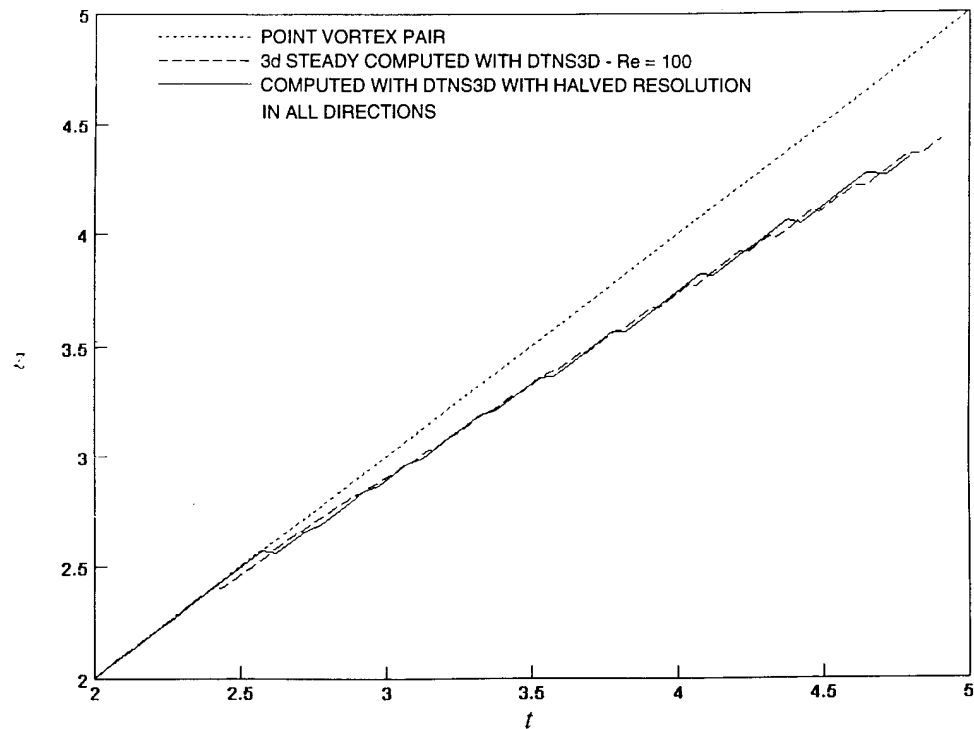


Fig. 18. Vertical location of vortex pair versus time computed with different grid resolutions.

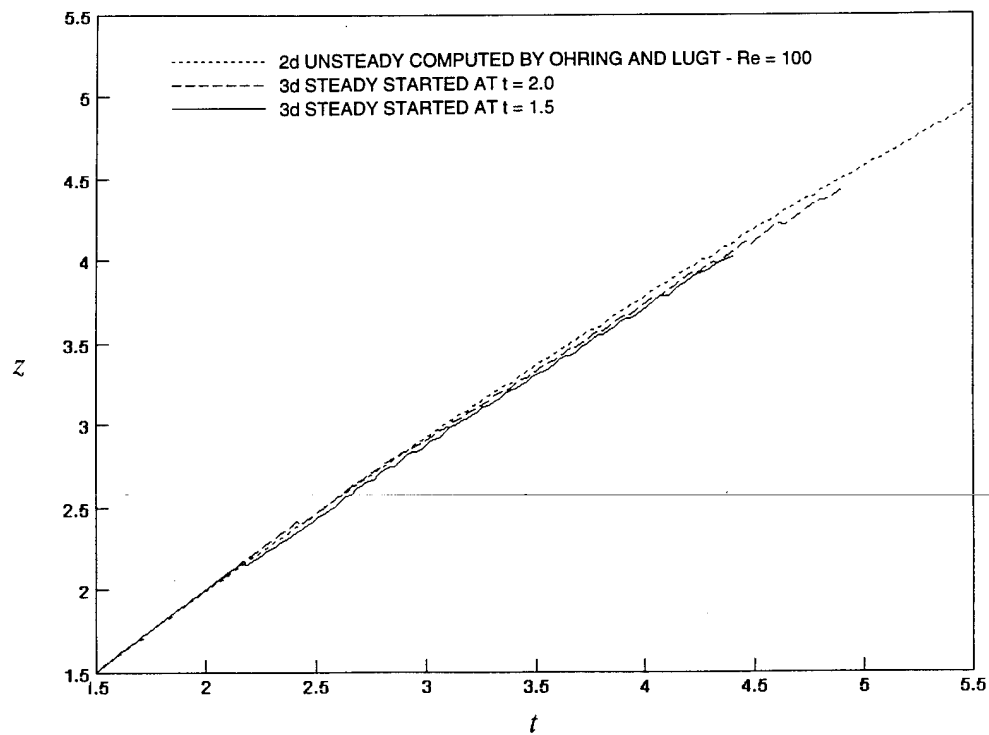


Fig. 19. Vertical location of vortex pair versus time computed with different starting times.

A third possible explanation for the deviation from the two-dimensional unsteady results lies in legitimate three-dimensional effects. One such effect is the generation of streamwise velocity gradients through the axial momentum balance. For example, Figures 20 and 21 show computed axial velocity contours at two x locations. At $x = 12.5$ the computed axial velocity shows a minimum between 9.6 and 9.7 near the vortex centers and a region of increased velocity with a maximum between 10.1 and 10.2. By $x = 25$ the contours are similar but the local maximum has decreased to below 10.1. This three-dimensional effect is certainly small but could have some influence on the rise velocity. To further assess this influence, additional computations are carried out with uniform inflow axial velocities of 5 and 100. As already shown for the single vortex, three-dimensional effects are enhanced by a decrease of axial velocity. Figure 22 shows a comparison of the computed rise histories for the three axial flow rates. The rise of the vortices is lowest for the smallest axial inflow ($U_0 = 5$). In that case, more axial vorticity is converted to tangential vorticity resulting in a reduced tangential velocity and thus a reduced upward velocity of the vortex pair. On the other hand, the largest axial flow case ($U_0 = 100$), exhibits the highest rise. This result clearly demonstrates the nature of the two-dimensional unsteady flow as the limit of the three-dimensional steady flow with infinite axial velocity. It also shows that for trajectories of the length of those considered here, the crossflow analogy yields a very good estimate of the vortex pair position as long as $U_0 \geq 10$.

VORTEX PAIR WITH NONUNIFORM AXIAL INFLOW

To investigate the effect of axial velocity variations on the rise of the pair, computations are carried out with an axial velocity inflow given by Batchelor's approximate solution (Equation 7) with the constant C chosen such that the axial velocity is zero at the inflow vortex centers. As for a single vortex with this axial flow variation, part of the tangential vorticity inherent in this distribution is quickly converted axial vorticity. However, as shown in Figure 23, this increased axial vorticity (and corresponding tangential velocity), is initially confined to the vicinity of the vortex core and has little influence on the rise-velocity of the pair. Later, as the increased axial vorticity spreads, the rise-velocity and vertical location of the pair noticeably exceeds that of the pair with uniform axial flow. It is interesting that the overall reduction of uniform axial flow results in a reduction in the rise of the pair (Figure 22), while the local reduction of the axial flow in the vortex cores results in an increase in the rise of the pair (Figure 23).

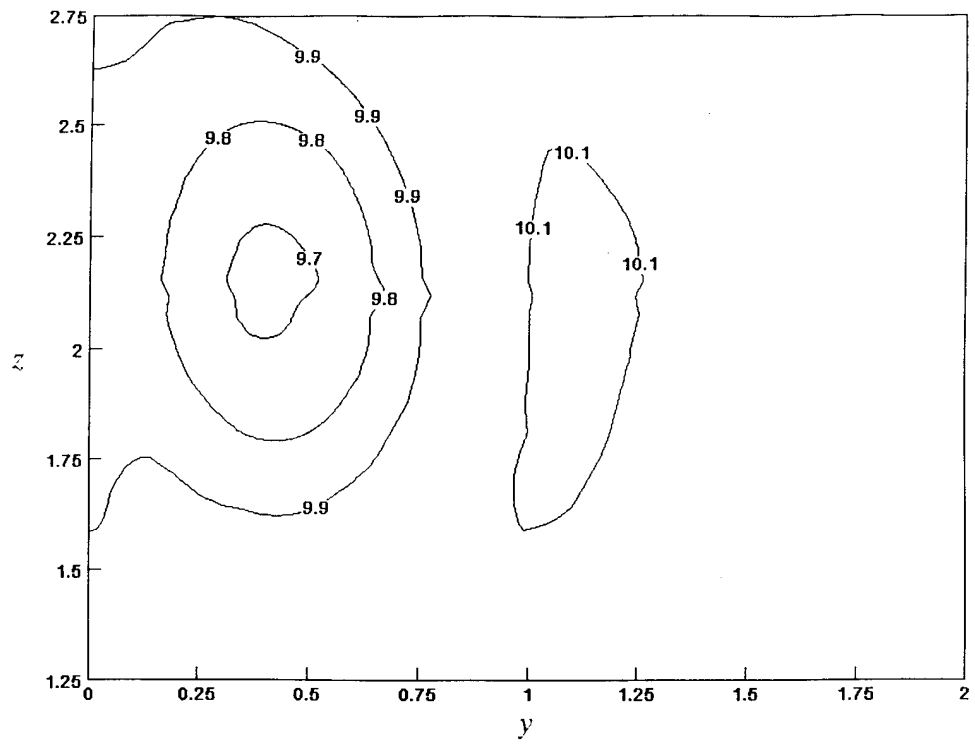


Fig. 20. Computed axial velocity contours at $x = 12.5$ for a vortex pair.

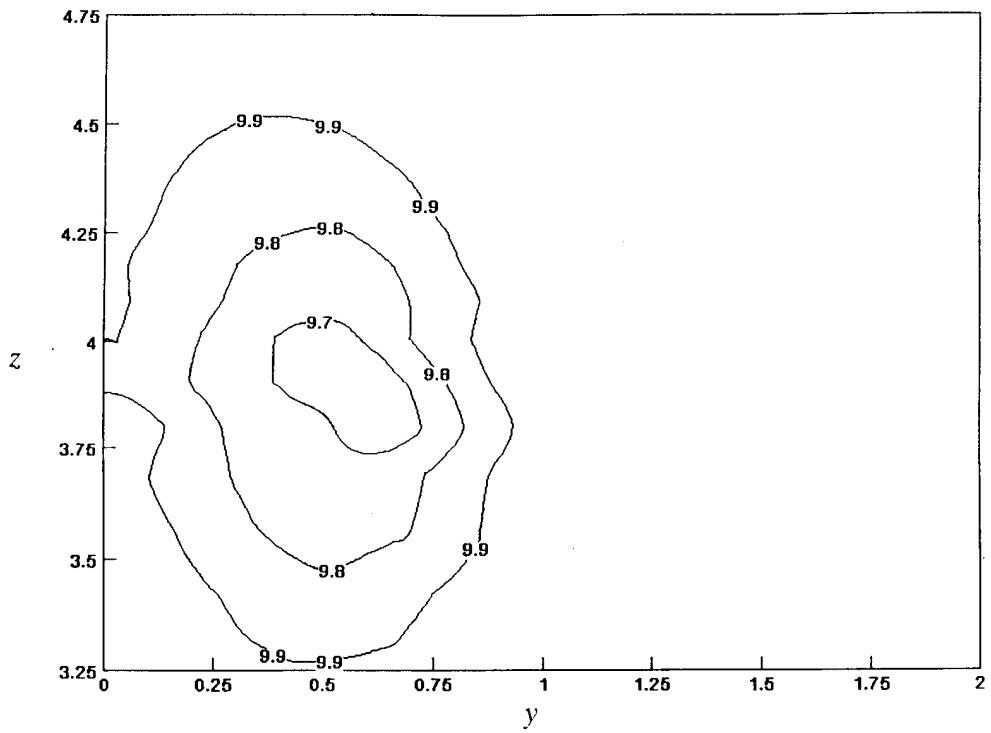


Fig. 21. Computed axial velocity contours at $x = 25$ for a vortex pair.

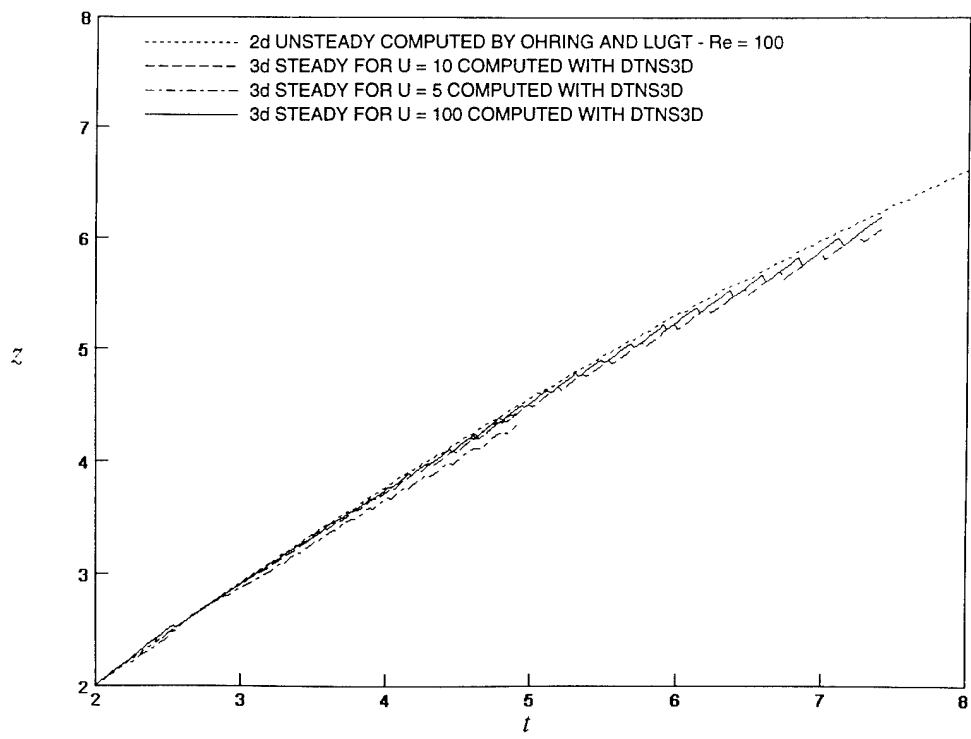


Fig. 22. Vertical location of vortex pair versus time computed with different axial flow rates.

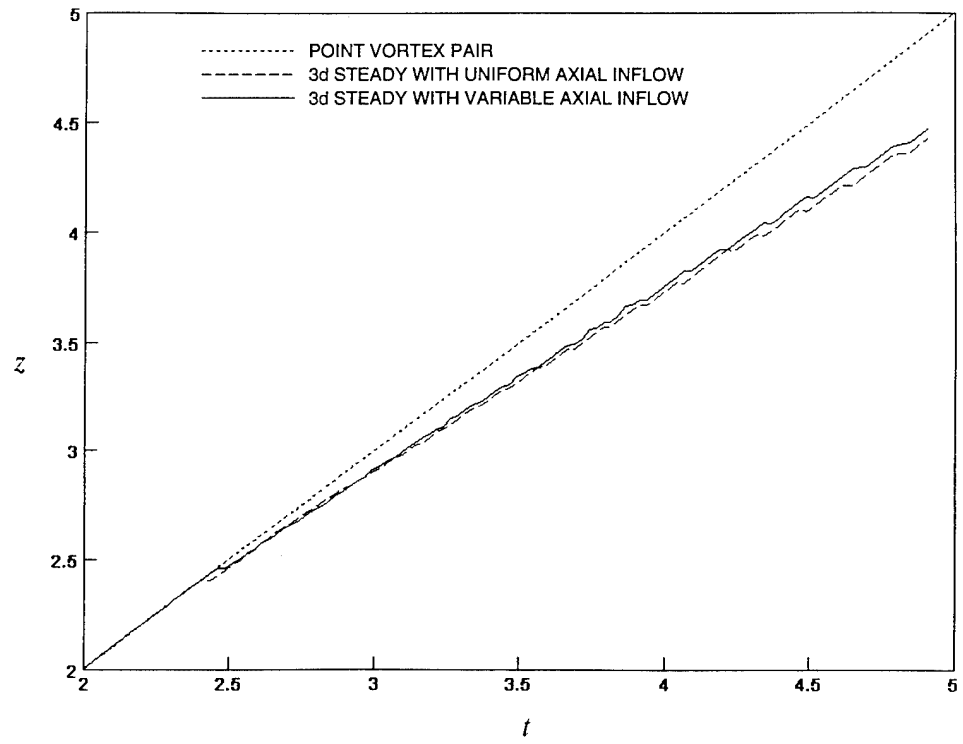


Fig. 23. Vertical location of vortex pair versus time computed with different axial flow distributions.

CONCLUSIONS AND RECOMMENDATIONS

A general-purpose RANS computer code has been tested for its ability to track isolated trailing vortices and vortex pairs. It is shown, through comparison with analytic solutions and previous computations, that the code can accurately locate such vortices at least for the case of laminar flow and for cases where turbulent flow is adequately modeled with a constant eddy viscosity. Computations with spatially varying inflow axial velocity demonstrate the effect of this flow component including its impact on the validity of the unsteady crossflow analogy.

Many vortices of practical interest are turbulent, and the constant eddy viscosity model of turbulence is too crude for their accurate treatment. For this reason, it is desirable to extend this work to a detailed study of turbulent trailing vortices. The impact of currently used turbulence models on the computational results can be assessed. Other promising models can be tested. The absence of analytic solutions and the shortage of detailed measured data will be a problem. A goal will be the selection or development of a model that adequately reflects the physics of these flow structures. Such a turbulence model implemented in a RANS code with an accurate vortex tracking capability such as demonstrated in this work will provide a valuable computational design tool.

ACKNOWLEDGMENTS

The computations were carried out at the U.S. Navy Submarine Hydrodynamics/Hydroacoustics Technology Center. The author benefitted from numerous stimulating discussions with Dr. Hans J. Lugt and would like to thank Mr. Samuel Ohring for providing his computational results for comparison.

THIS PAGE INTENTIONALLY LEFT BLANK

REFERENCES

1. Ohring, S. and H.J. Lugt, "The Decay of a Pair of Point Vortices in a Viscous Fluid," *Phys. Fluids A* 5, pp. 3299-3301 (1993).
2. Chakravarthy S.R. and S. Osher, "A New Class of High Accuracy TVD Schemes for Hyperbolic Conservation Laws," AIAA Paper No. 85-0363 (1985).
3. Gorski, J.J., "Solutions of the Incompressible Navier-Stokes Equations Using an Upwind-differenced TVD Scheme," in Lecture Notes in Physics, Vol. 323 (Ed. Dwyer, D.L., Hussaini, M.Y. and R.G. Voigt), pp. 278-282, *Proceedings of the 11th International Conference on Numerical Methods in Fluid Dynamics*, Williamsburg, VA (1988); Springer-Verlag, Berlin and Heidelberg, Germany (1989).
4. Gorski, J.J., "TVD Solutions of the Incompressible Navier-Stokes Equations with an Implicit Multigrid Scheme," AIAA Paper No. 88-3699, in *Proceedings of the AIAA/ASME/SIAM/APS First National Fluid Dynamics Congress*, Vol. 1, pp. 394-401 (1988); American Institute of Aeronautics and Astronautics, Washington, DC (1988).
5. Gorski, J.J., "Incompressible Cascade Calculations Using an Upwind Differenced TVD Scheme," in *Advances and Applications in Computational Fluid Dynamics* (Ed. O. Baysal), Vol. 66, pp. 61-69, *Proceedings of the ASME Winter Annual Meeting*, Chicago, IL (1988); American Society of Mechanical Engineers, New York (1988).
6. Gorski, J.J., S.R. Chakravarthy, and U.C. Goldberg, "High Accuracy TVD Schemes for the $k-\epsilon$ Equations of Turbulence," AIAA Paper No. 85-1665 (1985).
7. Batchelor, G.K., "Axial Flow in Trailing Line Vortices," *J. Fluid Mech.* 20, pp. 645-658 (1964).
8. Abramowitz, M. and I.A. Stegun., *Handbook of Mathematical Functions*, p. 228, Dover Publications, New York (1972).

THIS PAGE INTENTIONALLY LEFT BLANK

INITIAL DISTRIBUTION

Copies	Code	Name	Copies	Code	Name
1	ARPA	G. Jones	1	JHU Applied Physics Lab.	
			1		R. Thompson
4	ONR				
1	333	J. Fein			DIVISION DISTRIBUTION
1	333	S. Lekoudis			
1	333	P. Purtell	Copies	Code	Name
1	333	E. Rood	1	0114	K.-H. Kim
1	334	R. Vogelsong	1	2040	M. Hurwitz
1	NRL	W. Sandberg	1	2040.1	H. Lugt
			1	2041	S. Ohring
4	NAVSEA		1	2041	J. Slomski
1	03H	E. Comstock	1	2041	J. Telste
1	03HD	S. Petrie	1	2041	R. VanEseltine
1	03H3	H. Chatterton	1	2043	S. Willner
1	03H3	C. Chen	1	3421	TIC (C)
1	NUWC	P. Lefebvre	2	3432	Reports Control
1	OPNAV		1	50	W. Morgan
1	N87T	J. Schuster	1	50	D. Goldstein
			1	50	R. Ames
1	C.S. Draper Laboratory		1	512	T.C. Tai
1		T. Tureaud	1	52	W.-C. Lin
			1	521	P. Chang
2	Science Applications		1	521	W. Day
	International Corp.		1	521	C. Lin
1		N. Salvesen	1	521	T. Ratcliffe
1		R. Korpus	1	522	M. Wilson
			1	54	T. Huang
1	Mass Inst. of Tech./ Dept. of		1	54	B. Webster
	Ocean Eng.		1	5402	A. Reed
1		J. Kerwin	1	542	J. Busby
			1	542	R. Coleman
1	PSU Applied Res. Lab.		1	542	J. Gorski
1		C. Knight	10	542	H. Haussling
			1	542	Y.-T. Lee
1	Newport News Shipbuilding		1	542	G. Smith
1		M. Kim	1	544	F. Peterson
			1	544	C. Dai
1	Bolt, Beranek & Neuman		1	544	C.-I. Yang
1		S. Breit	1	56	D. Cieslowski
			1	564	J. Feldman
1	NorthWest Research Associates		1	564	M. Martin
1		D. Delisi	1	7051	W. Blake
1	General Dynamics		1	804	E. Quandt